Contract No.:

This manuscript has been authored by Battelle Savannah River Alliance (BSRA), LLC under Contract No. 89303321CEM000080 with the U.S. Department of Energy (DOE) Office of Environmental Management (EM).

Evaluation of crystalline quality of traveling heater method (THM) grown $Cd_{0.9}Zn_{0.1}Te_{0.98}Se_{0.02}$ crystals

U. N. Roy[1], J. N. Baker[1], G. S. Camarda[2], Y. Cui[2], G. Yang[3] and R. B. James[1]
[1]Savannah River National Laboratory, Aiken, SC 29808, USA.
[2]Brookhaven National Laboratory, Upton, NY 11973, USA.
[3]North Carolina State University, Raleigh, NC 27695, USA.

ABSTRACT

Because of its excellent opto-electronic properties, CdZnTe (CZT) has been the material of choice for X- and gamma-ray detectors operable at room temperature. CZT is the leading commercially available room-temperature radiation detector material today. Although a lot of progress has been made over the past three decades, today's CZT crystals still faces certain challenges, especially the presence of the performance-limiting materials defects and the associated relatively high production cost. In this regard $Cd_xZn_{1-x}Te_ySe_{1-y}$ (CZTS) is emerging as a next-generation compound semiconductor, which overcomes some of the limitations of CZT technology for the stated applications. Here, we conducted a study to evaluate the crystalline quality of traveling heater method (THM) grown CZTS with an optimized alloy composition, i.e., $Cd_{0.9}Zn_{0.1}Te_{0.98}Se_{0.02}$. The as-grown samples were evaluated by low-temperature photoluminescence (PL) spectroscopy and high-resolution X-ray diffraction using the synchrotron light source at Brookhaven National Laboratory (BNL). The full width at half maximum (FWHM) of both the PL and X-ray rocking curves were observed to be broadened due to the lattice disorder of the quaternary compound, eventually degrading the crystalline quality. This was consistent with Density Functional Theory (DFT) calculations.

Room-temperature nuclear radiation detectors enable a wide range of applications from astronomy and astrophysics, medical imaging, high energy physics, homeland security and non-proliferations [1-7]. The room-temperature radiation detector materials mainly fall into two different categories based on their operating principle: scintillators and semiconductors. Semiconductor-based detectors have several advantages over scintillator materials. The detectors based on semiconductors offer better energy resolution and proportionality over a wide range of energy, ranging from few keV to MeV. The requirements of the semiconductor materials for these applications, however, are stringent, and all these applications demand very high-quality detectors at a reasonably low cost. In this regard CdZnTe (CZT) is the leading semiconductor material and has been developed for more than three decades due to its favorable physical and optoelectronic properties [8-13]. CZT offers an optimum band gap to achieve high resistive material and ensure a very low dark current, is capable of absorbing high-energy photons to create sufficient photo-generated carriers and possesses excellent charge transport properties. However, despite continuous improvements for the last three decades or more, the material still suffers from a few persistent long-standing issues. As a result, the deployment of large-volume CZT detectors at reasonably low cost is still challenging. The compositional homogeneity of CZT ingots is compromised due to the non-unity segregation coefficient of Zn in the CdTe matrix[14], limiting the availability of large-volume detectors at low cost. The other two major issues associated with CZT technology are a high concentration of Te inclusions and an extensive sub-grain boundary network. These defects pose severe detrimental effects to the charge transport properties and are the root cause for spatial inhomogeneity of charge transport properties of the material, which eventually degrades the device performance harshly[15-18]. All these long-standing issues hampers the production of high-energy-resolution CZT detectors at low cost of production and thus limits the widespread use of the material.

Recently, replacing Te with a small amount of selenium (Se) in the CZT matrix was revealed to overcome the above said limitations of present-day CZT technology. As a result, the resulting quaternary $Cd_{1-x}Zn_xTe_{1-y}Se_y$ (CZTS) crystals are being actively studied as a promising material with a competitive production cost for next generation room temperature X-ray and gamma-ray detectors [19-27]. Addition of selenium to the CZT matrix was found to lead to multi-pronged advantages. First the selenium was found to have influence on modifying the Zn segregation coefficient to near unity, resulting in improved compositional homogeneity for Bridgman-grown, gradient freeze-grown and THM-grown CZTS ingots [19, 20,28,29,] as compared to conventional CZT. Chang et al. [30] reported uniform composition for $Cd_{0.96}Zn_{0.04}Te_{0.84}Se_{0.16}$ ingots grown by the vertical Bridgman technique. The new quaternary material is reported to be free from sub-grain boundary networks [31-33] as Se acts as an effective lattice hardening agent in CZTS matrix. The sub-grain boundary network is known to be the major performance-limiting defect in CZT material [12]. Secondly, relatively low concentrations of Te inclusions have been observed in CZTS materials irrespective of growth techniques [24,29,34-35] together with reduced concentrations of electrically active defects [36] and increased mechanical hardness [37]. Thus, Se can act as an effective defect engineering element in the CZTS matrix to mitigate the long-standing issues pertaining to CZT materials. However, the addition of Se in CdTe or CZT matrix could impose severe compositional disorder at the atomic or microscopic level, and it is responsible for

bandgap bowing [38,39]. The effects of alloy disorder on the crystalline quality were addressed in this present report. Recently, we observed that CZTS with 10% Zn and 2% Se is the optimum composition regarding the best charge transport properties [40]. In this paper we report an effort to understand the crystalline quality of THM-grown $Cd_{0.9}Zn_{0.1}Te_{0.98}Se_{0.02}$ sample using low-temperature photoluminescence (PL) spectroscopy, high resolution X-ray diffraction (HRXRD) and theoretical density functional theory (DFT) calculations to better understand the effects of alloy disorder.

$Cd_{0.9}Zn_{0.1}Te_{0.98}Se_{0.02}$ crystals doped with indium (In) were grown by the Traveling Heater Method (THM). It is to be noted that cadmium vacancy was found to be less in CZTS compared to CZT[36]. Thus, the concentration of indium dopant required to compensate in order to achieve high resistivity is expected to be less than for CZT[29]. The growth procedure is detailed elsewhere[20]. The as-grown ingot was cut into wafers of different dimensions for various characterizations using a programmable diamond wire saw. The samples were lapped and polished to mirror surface-finish after final polishing with 0.05-µm alumina suspension on a felt pad. Low-temperature (~4.2K) photoluminescence (PL) spectroscopy was used to evaluate the quality of the materials. For PL measurements, the samples were excited with a laser beam of wavelength 488 nm, and the PL signal was dispersed by an iHR550 spectrometer purchased from Horiba Scientific. The PL setup used for the present study is detailed elsewhere [41]. The high-resolution X-ray diffraction (HRXRD) study was carried out at NSLS-II beam line 4-ID at BNL. The monochromatic beam energy used for the diffraction measurements was 7.11 keV with a beam size of 0.50x0.05 mm^2. For the low-temperature PL and high-resolution X-ray diffraction measurements, the polished samples were etched with freshly prepared 2% bromine-methanol solution for two minutes to remove the damaged surface layer caused by the polishing process. The density functional theory (DFT) simulations were performed on a series of special quasi-random structures (SQS) with alloy composition near that of the experimental samples. The Alloy Theoretic Automated Toolkit's Monte Carlo SQS module was used to generate the structures, while VASP was used to perform the DFT simulations for relaxing the volume and atomic geometries[42-48]. The Perdew, Burke, Ernzerhof (PBE) exchange correlation functional, along with a plane wave kinetic energy cutoff of 520 eV, 2x2x2 Monkhorst Pack kpoint mesh, and Projector-Augmented-Wave (PAW) pseudopotentials, were used for all calculations, with 12 electrons explicitly modeled for cadmium and zinc and 6 for tellurium and selenium.

The low-temperature PL is a proven, powerful technique to qualitatively evaluate the crystalline quality of as-grown materials, especially for semiconductors. A typical PL spectrum of as-grown $Cd_{0.9}Zn_{0.1}Te_{0.98}Se_{0.02}$ sample registered at 4.2K is displayed in Figure 1a. It resembles the spectra typical of high-quality $Cd_{0.9}Zn_{0.1}Te$ [1, 41,49-53]. The PL spectrum in general can be divided into three regions including Region (I): 1.617 eV to 1.67 eV, which is the exciton region, region (II): 1.54 eV to 1.617 eV, the donor-acceptor pair recombination region and region (III): 1.3 eV to 1.54 eV is the defect band, generally known as the A-center. Region (I) is perhaps the most important part of the PL spectrum, since it reflects the crystalline quality of the material. The enlarged version of region I along with the deconvolution are shown in Fig. 1b. The PL spectrum contains the free exciton line, and the appearance of the free excitons itself demonstrates high crystalline quality of the CZTS sample. The emission line at 1.6474 eV, denoted by $(X)_{n=1}$ (Fig 1b), is due to the recombination of free excitons in their ground state, while the X_{up} emission line at 1.6503 eV is due to the upper branch of the exciton-polariton

excitation and was also observed earlier for high-quality CZT [49,52,53]. The neutral donor-bound exciton (D^0, X) is the most dominant peak and is also common in CZT samples. The energy position of the (D^0, X) peak was observed at 1.6452 eV with full width half maximum (FWHM) of about 3.2 meV. The neutral acceptor-bound exciton, commonly denoted as (A^0, X), was observed at the energy position of 1.6287 eV. The peak assigned as (A^0, X-1LO) as shown in Fig. 1a, is the phonon replica of (A^0, X), where the separation of the phonon replica is reported to be about 22 meV [52]. The emission peak at 1.583 eV is due to donor-acceptor pair recombination and is denoted as (DAP). The broad band centering around 1.461 eV is commonly known as the A-center[1], and it originates from the Cd-vacancy-donor complex; in the present case it is the Cd-vacancy-In complex. The FWHM value of the (D^0, X) peak also a good figure of merit for the crystallinity, and it portrays the nature of the material qualitatively. A value of about 2.2 meV has been reported earlier for THM-grown CZT[52]. In the present case for CZTS, the FWHM value obtained for the (D^0, X) peak was 3.2 meV. Although the $Cd_{0.9}Zn_{0.1}Te_{0.98}Se_{0.02}$ crystals were grown with similar growth conditions as for CZT growth by THM[20], and the same PL setup was used for both CZT and CZTS samples, the relatively broader FWHM of the (D^0, X) peak of CZTS compared to CZT is feasibly due to the compositional disorder (viz. the lattice disorder because of adding selenium to the CZT matrix).

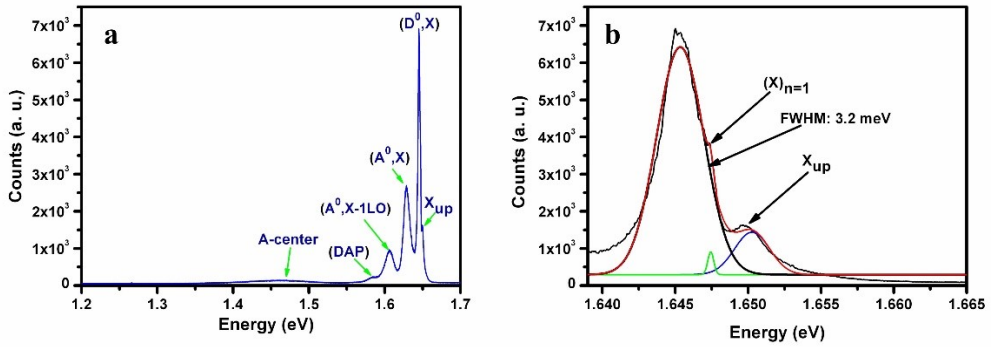

Figure 1. a) Low-temperature (4K) photoluminescence spectrum of as-grown $Cd_{0.9}Zn_{0.1}Te_{0.98}Se_{0.02}$ sample and b) enlarged version of (D^0, X) peak.

It is well known that the band gap decreases with added Se (for up to ~40% Se) in CdTe/CZT matrix because of compositional/lattice disorder[38,39], even though the band gap of CdSe is higher than CdTe/CZT. This decrease of band gap is commonly known as band gap bowing. A high-resolution X-ray diffraction experiment was carried out for the as-grown $Cd_{0.9}Zn_{0.1}Te_{0.98}Se_{0.02}$ sample using the NSLS-II beam line 4-ID at BNL. The high-resolution X-ray rocking curve for the as-grown $Cd_{0.9}Zn_{0.1}Te_{0.98}Se_{0.02}$ sample is shown in Fig. 2 for the (220) plane. The presence of any low angle grain boundary/sub-grain boundaries gives rise to the appearance of multiple peaks, and the separation of the peaks corresponds to the tilt angle[54].

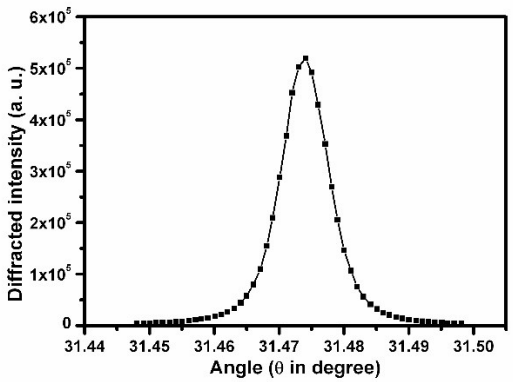

Figure 2. High resolution X-ray rocking curve of an as-grown $Cd_{0.9}Zn_{0.1}Te_{0.98}Se_{0.02}$ sample grown by THM.

The symmetrical single diffraction curve with a FWHM of 30.8 arc-sec represents good crystalline quality of the CZTS material and depicts the absence of any mosaic structure. There is large dispersion in the reported values of FWHM for CZT in the literature ranging from >100 arc-sec to ~8 arc-sec[55-61]. Chang et al.[30] also observed a lattice disorder broadening effect on Se addition in CZT matrix as evaluated by double crystal X-ray diffraction study. The defect densities, sub-grain boundary network, residual stress, surface disorder, and presence of Te inclusions near the sample surface can have significant contribution towards broadening of the XRD peak. It is to be noted that, qualitatively, we did not observe the presence of considerable residual stress in any of our CZTS samples with selenium concentrations ranging from 2-7%, as characterized by X-ray topography and infrared (IR) transmission investigation through crossed polarizers[19-21,26, 31,32]. The ingots were also found to be stress free, and no lattice distortion was observed near the periphery of the wafer touching the ampoule wall[19,32]. The CZTS samples were free from sub-grain boundary networks and observed to contain a very low amount of Te inclusions compared to typical CZT. Thus, the FWHM value for CZTS is expected to be lower than the observed value, principally due to the absence of a sub-grain boundary network. The relatively higher FWHM value is possibly induced by lattice disorder. The FWHM of the X-ray diffraction curve was found to increase from 70 arc-sec to 107 arc-sec after adding 16 atomic % Se in the $Cd_{0.96}Zn_{0.04}Te$ matrix for the same surface processing conditions, reflecting the degradation of the crystalline quality for these higher Se concentrations[30]. The FWHM for high-quality THM-grown commercial grade CZT was reported to be about 40 arc-sec[61].

The disorder in the CdTeSe or CdZnTeSe lattices do not appear to have an adverse effect on the device performance. For example, in CdTeSe, the electron effective mass is reported to decrease with selenium concentration suggesting an enhanced electron mobility. Moreover, CdTeSe based solar cells were found to be more efficient as compared to CdTe-based ones, and the minority carrier lifetime for CdTeSe layers was reported to be enhanced sixfold compared to CdTe layers[62,63]. Fiederle et al.[64] reported a higher charge collection efficiency for CdTeSe-based radiation detectors as compared to CdTe.

Table 1: Summary of representative bond length statistics from a subset of the SQS simulations

Composition	Bond type	Bond length (Å)		Ideal (110) spacing (Å)	
		Mean	Stnd. dev	Mean	Stnd. dev
$Cd_{.9074}Zn_{.0926}Te$	***Zn-Te***	2.7119	0.0077	4.4285	0.0098
	Cd-Te	2.8657	0.0077	4.6797	0.0098
$Cd_{.9074}Zn_{.0926}Te_{.9815}Se_{.0185}$	***Zn-Te***	2.7123	0.0114	4.4291	0.0145
	Cd-Te	2.8651	0.0094	4.6786	0.0120
	Cd-Se	2.7267	0.0020	4.4527	0.0026

In order to better understand the origin of the relatively higher FWHM value in the rocking curve, DFT calculations were performed to estimate the bond length/lattice disorder in the quaternary matrix. Structures with tetragonal supercells were prepared at compositions of $Cd_{.9074}Zn_{.0926}Te$ (108 atom), $Cd_{.9074}Zn_{.0926}Te_{.9815}Se_{.0185}$ (108 atom), and pure CdTe and ZnTe (72 atom). The SQSs were generated with pair correlations out to 2nd nearest-neighbor shells. Two SQS simulations were performed for each non-zero Se content, due to the low number of Se atoms in supercells of this size. The bond length statistics of the more representative of these two sets are listed in Table 1, while the idealized (110) interplanar spacings calculated from these distributions are plotted in Figure 3. The ideal (110) spacing is the interplanar spacing of a corresponding zincblende unit cell composed solely of the given bond length. No Zn-Se bonds were present in the simulated composition due to the random population of the SQS matrix. As indicated in the table, alloying CdTe with ZnTe leads to an overall lengthening of ZnTe bonds and an overall shortening of CdTe bonds. This is because ZnTe tetrahedra in the CdTe matrix introduce solute strain fields, causing distortions that propagate through neighboring cells. This introduces random scatter in the bond lengths in and around these strain fields (in other words, alloy scattering/alloy disorder) and, correspondingly, in the interplanar spacings. Upon addition of Se, this scatter increases further, with the composition-weighted standard deviation of the Te bond lengths increasing from 0.0077 with no Se to 0.0094 and 0.0114, respectively, in the two 1.85% Se simulations, and from 0.0098 to 0.012 and 0.0145 for the (110) spacings. The alloy disorder was found to be enhanced with increased selenium in the matrix while keeping Zn constant.

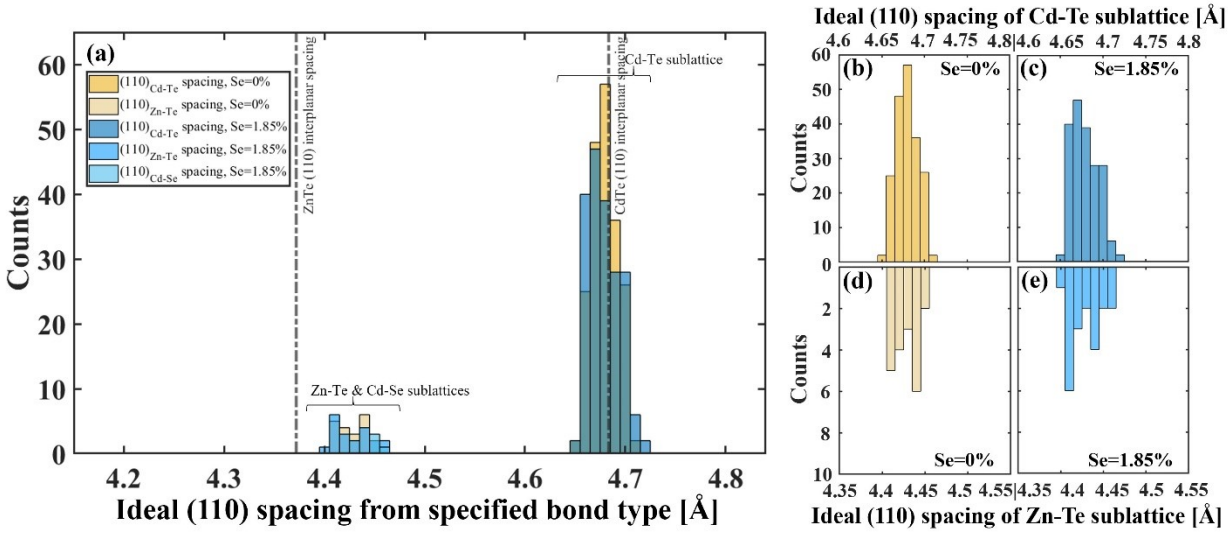

Figure 3: Representative statistics of $Cd_{.9074}Zn_{.0926}Te$ and $Cd_{.9074}Zn_{.0926}Te_{.9815}Se_{.0185}$ alloy SQS simulations shown as ideal (110) interplanar spacing binned into 0.01 Å bins. Counts are bonds of atoms within this simulation volume corresponding to the given (110) spacing bin. (a) Calculated interplanar spacings showing Cd-Te, Cd-Se, and Zn-Te sublattice spacings. Vertical dashed lines show the bond lengths in pure ZnTe and pure CdTe. Here, the sublattice interplanar spacing statistics are broken out by composition (columns) and sublattice type (rows). (b,c) Cd-Te sublattice statistics and (d,e) Zn-Te sublattice statistics.

Table 1 shows the bond length and idealized (110) spacing statistics for Se=0% and Se=1.85% compositions, broken out by bond type. The overall statistics can be recovered by taking the composition-weighted average of these quantities. Figure 3 shows the same data, in the form of histograms, to visually show the changes in the distributions upon addition of Se. The histograms in Figure 3 are color coded: tan graphs correspond to Se=0%, and blue graphs correspond to Se=1.85%, with the lightness of the color indicating the specific sublattice. Figure 3a shows a summary view of all ideal (110) spacings, while Figures 3b-e show breakouts organized by row and column. The rows correspond to the sublattice type (Figs. 3b and 3c are Cd-Te, and 3d and 3e are Zn-Te), while the columns correspond to Se content (Figs. 3b and 3d are for Se=0%, while Figs. 3c and 3e are for Se=1.85%).

The composition weighted standard deviations and the mechanism governing them are central to understanding the degradation of crystalline quality evaluated by low-temperature PL and high resolution XRD, since the ratios of these standard deviations show how the FWHM of the HR-XRD and low-temperature PL are expected to intrinsically vary for otherwise identical crystals. The observed investigation suggested a lattice disorder induced degradation of the crystalline quality. Our DFT calculations also suggested that the degradation of crystalline quality was due to the inherent existence of lattice disorder in the Se containing quaternary. The changes in alloy scatter/disorder upon addition of Se may be understood geometrically. The difference in ideal ZnTe and CdTe bonds means that bond distortions are already present across the entire lattice due to overlapping solute strain fields. Introduction of even small amounts of Se to this matrix therefore causes changes that propagate through the entire structure, resulting in degradation of crystalline quality, which is observable as the increased FWHM in CZTS vs. CZT.

This work was partially supported by the U.S. Department of Energy, Office of Defense Nuclear Nonproliferation Research and Development, and the Laboratory Directed Research and Development (LDRD) program within the Savannah River National Laboratory (SRNL). This work was produced by Battelle Savannah River Alliance, LLC under Contract No. 89303321CEM000080 with the U.S. Department of Energy. The publisher acknowledges the U.S. Government license to provide public access under the DOE Public Access Plan (http://energy.gov/downloads/doe-public-access-plan). We would like to thank Christie Nelson for her support of the High-resolution X-ray diffraction experiment at NSLSII beam line 4-ID at BNL.

References:

1. T.E. Schlesinger, J.E. Toney, H. Yoon, E.Y. Lee, B.A. Brunett, L. Franks and R.B. James, Materials Science and Engineering R **32**, 103 (2001).
2. G. Yang and R. B. James, in Physics, Defects, Hetero- and Nano- Structures, Crystal Growth, Surfaces and Applications: Part II, EDAX, edited by R. Triboulet et al. (Elsevier, 2009), p. 214.
3. S.D. Barthelmy, L.M. Barbier, J.R. Cummings, E.E. Fenimore, N. Gehrels, D. Hullinger, H.A. Krimm, C.B. Markwardt, D.M. Palmer, A. Parsons, G. Sato, M. Suzuki, T. Takahashi, M. Tashiro, and J. Tueller, Space Science Reviews **120**, 143 (2005).
4. J. Tang, F. Kislat, and H. Krawczynski, Astroparticle Phys. 128, 102563 (2021).
5. K. Iniewski, J. of Instrumentation **11**, C12034 (2016).
6. M.F. Santarelli, G. Giovannetti, V. Hartwig, S. Celi, V. Positano, and L. Landini, Electronics **10**, 1642 (2021).
7. Md D. Alam, S.S .Nasim, and S. Hasan, Prog. In Nuclear Energy **140**, 103918 (2021).
8. M.C. Veale, P. Booker, S. Cross, M.D. Hart, L. Jowitt, J. Lipp, A. Schneide, P. Seller, R.M. Wheater, M.D. Wilson, and C.C.T. Hansson, Sensors **20**, 2747 (2020).
9. H. Chen, S.A. Awadalla, K. Iniewski, P.H. Lu, F. Harris, J. Mackenzie, T. Hasanen, W. Chen, R. Redden, G. Bindley, I. Kuvvetli, J. Appl. Phys. **103**, 014903 (2008).
10. R. B. James, B. Brunett, J. Heffelfinger, J. Van Scyoc, J. Lund, F.P. Doty, C.L. Lingren, R. Olsen, E. Cross, H. Hermon, H. Yoon, J. Electron. Materials **27**, 788 (1998).
11. U.N. Roy, S. Weiler, J. Stein, M. Groza, V. Buliga, and A. Burger, IEEE Trans. Nucl. Sci. **58**, 1949 (2011).
12. A.E. Bolotnikov, G.S. Camarda, Y. Cui, G. Yang, A. Hossain, K. Kim, and R.B. James, J. Cryst. Growth 379, 46 (2013).
13. A. Burger, M. Groza, Y. Cui, U.N. Roy, D. Hillman, M. Guo, L. Li, G.W. Wright, R.B. James, Phys. Status Solidi C **2**, 1586 (2005).
14. N. Zhang, A. Yeckel, A. Burger, Y. Cui, K.G. Lynn, and J.J. Derby, J. Cryst. Growth **325**, 10 (2011).
15. G. A. Carini, A. E. Bolotnikov, G. S. Camarda, and R. B. James, Nucl. Instrum. Methods Phys. Res., Sect. A **579**, 120 (2007).
16. M. Amman, J. S. Lee, and P. N. Luke, J. Appl. Phys. **92**, 3198 (2002).
17. G.S. Camarda, A.E. Bolotnikov, Y. Cui, A. Hossain, S.A. Awadalla, J. Mackenzie, H. Chen, R.B. James, IEEE Trans. Nucl. Sci. **55**, 3725 (2008).
18. A. Hossain, A.E. Bolotnikov, G.S. Camarda, Y. Cui, R. Gul, U.N. Roy, G. Yang, R.B. James, J. Cryst. Growth **470**, 99 (2017).
19. U.N. Roy, G.S. Camarda, Y. Cui, R. Gul, A. Hossain, G. Yang, J. Zazvorka, V. Dedic, J. Franc, and R.B. James, Sci. Rep. **9**, 1620 (2019).
20. U.N. Roy, G.S. Camarda, Y. Cui, R. Gul, A. Hossain, G. Yang, J. Zazvorka, V. Dedic, J. Franc, and R.B. James, Sci. Rep. **9**, 7303 (2019).
21. U. N. Roy, G.S. Camarda, Y. Cui, and R.B. James, Appl. Phys. Lett. **114**, 232107 (2019).
22. S.K. Chaudhuri, M. Sajjad, and K.C. Mandal, Appl. Phys. Lett. **116**, 162107 (2020).
23. S.K. Chaudhuri, M. Sajjad, J.W. Kleppinger, and K.C. Mandal, J. Appl. Phys. **127**, 245706 (2020).
24. J.W. Kleppinger, S.K. Chaudhuri, U.N. Roy, R.B. James, and K.C. Mandal, IEEE Trans. Nucl. Sci. **68**, 2429 (2021).

25. A. Yakimov, D. Smith, J. Choi, and S. Araujo, SPIE Proc. **11114**, 111141N (2019).
26. V. Dědič, T. Fridrišek, J. Franc, J. Kunc, M. Rejhon, U.N. Roy, and R.B. James, Sci. Rep. **11**, 2154 (2021).
27. J. Pipek, M. Betušiak, E. Belas, R. Grill, P. Praus, A. Musiienko, J. Pekarek, U.N. Roy, R.B. James, Phys. Rev. Appl. **15**, 054058 (2021).
28. L. Martínez-Herraiz, A.F. Bra˜na, and J.L. Plaza, J. Cryst. Growth **537**, 126291 (2021).
29. S. Hwang, H. Yu, A.E. Bolotnikov, R.B. James, and K. Kim, IEEE Trans. Nucl. Sci. **66**, 2329 (2019).
30. C.Y. Chang and B. H. Tseng, Materials Sc. and Engr. B **49**, (1997) 1.
31. U.N. Roy, G.S. Camarda, Y. Cui, and R.B. James, Appl. Phys. Lett. **115**, 242102 (2019).
32. U.N. Roy, G.S. Camarda, Y. Cui, and R.B. James, J. Cryst. Growth **546**, 125753 (2020).
33. U.N. Roy, G.S. Camarda, Y. Cui, and R.B. James, Radiation **1**, 123 (2021).
34. S.U. Egarievwe, U.N. Roy, E.O. Agbalagba, B.A. Harrison, C.A. Goree, E.K. Savage, and R.B. James, IEEE Access **8**, 137530 (2020).
35. S.K. Chaudhuri, J.W. Kleppinger, O. Karadavut, R. Nag and K.C. Mandal, Crystals **11**, 827 (2021).
36. R. Gul, U.N. Roy, G.S. Camarda, A. Hossain, G. Yang, P. Vanier, V. Lordi, J. Varley, and R.B. James, J. Appl. Phys. **121**, 125705 (2017).
37. J. Franc, P. Moravec, V. Dědič, U. Roy, H. Elhadidy, P. Minárik, V. Šíma, Materials Today Comm. **24**, 101014 (2020).
38. L. Hannachi, N. Bouarissa, Superlattices and Microstructures **44**, 794 (2008).
39. K. Benkabou, N. Amrane, M. Maachou, Journal of Alloys and Compounds **465**, 305 (2008).
40. U. N. Roy, G. S. Camarda, Y. Cui, and R. B. James, Appl. Phys. Lett. **118**, 152102 (2021).
41. G. Yang, A.E. Bolotnikov, Y. Cui, G.S. Camarda, A. Hossain, K.H. Kim, R. Gul, and R.B. James, Appl. Phys. Lett. **98**, 261901 (2011).
42. A. van de Walle, M. Asta, and G. Ceder, Calphad **26**, 539 (2002).
43. A. van de Walle, Calphad **33**, 266 (2009).
44. A.van de Walle, P. Tiwary, M.de Jong, D.L. Olmsted, M. Asta, A. Dick, D. Shin, Y. Wang, L.-Q. Chen, and Z.-K. Liu, Calphad **42**, 13 (2013).
45. A van de Walle and M. Asta, Modelling and Simulation in Materials Science and Engineering **10**, 521 (2002).
46. G. Kresse and J. Furthmüller, Computational Materials Science **6**, 15 (1996).
47. G. Kresse and J. Furthmüller, Physical review B **54**, 11169 (1996).
48. G. Kresse and D. Joubert, Physical Review B **59**, 1758 (1999).
49. J. González-Hernández, E. López-Cruz, D.D. Allred, W.P. Allred, J. Vac. Sc. and Tech. A**8**, 3255 (1990).
50. I. Nasiekaa, N. Kovalenkob, V. Kutniyc, A. Rybkac. D. Nakonechnyjc, S. Sulimab, V. Strelchuka, Sensors and Actuators A **203**, (2013) 176.
51. H. Chen, J. Tong, Z. Hu, D. T. Shi, G. H. Wu, K.-T. Chen, M. A. George, W. E. Collins, and A. Burger, J. Appl. Phys. **80**, (1996) 3509.
52. U. N. Roy, S. Weiler, J. Stein, M. Groza, A. Burger, A. E. Bolotnikov, G. S. Camarda, A. Hossain, G. Yang, and R. B. James, MRS Proc. **1341**, (2011) 29.
53. K. Hjelt, M. Juvonen, T. Tuomi, S. Nenonen, E.E. Eissler, and M. Bavdaz, Phys. Stat. Sol. A **162**, (1997) 747.

54. M. Shkir, V. Ganesh, S. Al Faify, A. Black, E. Dieguez, G. Bhagavannarayana, J. Alloys and Compounds **686**, (2016) 438.
55. G.A. Carini, G.S. Camarda, Z. Zhong, D.P. Siddons, A.E. Bolotnikov, G.W. Wright, B. Barber, C. Arnone, and R.B. James, J. Electron. Materials **34**, 804 (2005).
56. D. Zenga, W. Jiea, T. Wanga, G. Zhaa, and J. Zhang, Nucl. Instrum. Methods A **586**, 439 (2008).
57. J.K. Markunas, L.A. Almeida, R.N. Jacobs, J. Pellegrino, S.B. Qadri, N. Mahadik and J. Sanghera, J. Electron. Materials **39**, 738 (2010).
58. V. Carcelen, K.H. Kim, G.S. Camarda, A.E. Bolotnikov, A. Hossain, G. Yang, J. Crocco, H. Bensalah, F. Dierre, E. Die´guez, and R.B. James, J. Cryst. Growth **338**, 1 (2012).
59. D. Brellier, E. Gout, G. Gaude, D. Pelenc, P. Ballet, T. Miguet, and M. C. Manzato, J. Electron. Materials **43**, 2901 (2014).
60. H. Yoon, J.M. Van Scyoc, M.S. Goorsky, H. Hermon, M. Schieber, J.C. Lund, and R.B. James, J. Electron. Materials **26**, 529 (1997).
61. J. Mackenzie, F.J. Kumar, and H. Chen, J. Electron. Materials **42**, 3129 (2013).
62. M. Lingg, S. Buecheler and A. N. Tiwari, Coatings **9**, 520 (2019).
63. J. Guo, A. M. Kanakkithodi, F. G. Sen, E. Schwenker, E. S. Barnard, A. Munshi, W. Sampath, M. K. Y. Chan, and R. F. Clie, Appl. Phys. Lett. **115**, 153901 (2019).
64. M. Fiederle, D. Ebling, C. Eiche, D. M. Hofmann, M. Salk, W. Stadler, K. W. Benz and B. K. Meyer, J. Cryst. Growth **138**, 529 (1994).